A mathematical model of a molten carbonate direct carbon fuel cell

Song, Datong; Xie, Zhong; Zhang, Xinge; Qu, Wei; Wang, Qianpu

Publisher's version / Version de l'éditeur:
https://doi.org/10.1149/2.0262001JES
Journal of The Electrochemical Society, 167, 1, pp. 1-13, 2019-12-12

A Mathematical Model of a Molten Carbonate Direct Carbon Fuel Cell

Journal of The Electrochemical Society, 2020 **167** 013526

A Mathematical Model of a Molten Carbonate Direct Carbon Fuel Cell

Datong Song, Zhong Xie,[z] Xinge Zhang, Wei Qu, and Qianpu Wang

Energy, Mining and Environment Research Centre, National Research Council Canada, Vancouver, B.C. V6T 1W5, Canada

A one-dimensional (1D) homogeneous unit cell model was developed to study the performance of the molten carbonate direct carbon fuel cell (DCFC), which uses solid carbon as fuel and molten carbonate as electrolyte. It is the first unit cell model for the molten carbonate DCFC in which both 4-electron carbon oxidation and 2-electron CO oxidation reactions, as well as the reverse Boudouard reaction, are considered. The simulation results verify that, besides the relatively sluggish kinetics of the anodic reactions, cell performance is mainly limited by ohmic losses in the anode. Further modeling exploration reveals that a minimum effective electronic conductivity of around 0.56 S/cm is required to facilitate proper electrical conduction in the cathode to attain high DCFC performance. It was found that there are optimal volume fractions for the carbon fuel and liquid electrolyte in the anode. If the effective electronic conductivity of the cathode falls to 0.56 S/cm, optimal volume fractions also exist for the solid material and liquid electrolyte in the cathode. The detailed modeling analysis showed that performance improvement at high operating temperature was mainly attributed to improvement of anodic kinetics and reduction of ohmic loss in the electrolyte of electrodes and electrolyte matrix.
 [DOI: 10.1149/2.0262001JES]

Manuscript submitted August 21, 2019; revised manuscript received October 31, 2019. Published December 12, 2019. *This paper is part of the JES Focus Issue on Mathematical Modeling of Electrochemical Systems at Multiple Scales in Honor of Richard Alkire.*

Power plants operating on fossil fuels, especially coal, provide more than 80% of global primary energy and release copious quantities of CO_2 and other contaminants into the environment.[1] Significant reduction of greenhouse gas (GHG) emission requires highly efficient technologies to convert carbonaceous solid fuels into electricity. A direct carbon fuel cell (DCFC) converts the chemical energy in the carbon fuel directly into electricity without gasification and is considered as one of the most promising and highly efficient technologies in power generation, CO_2 capture and sequestration.[2] Compared to conventional coal-fired power plants and to other fuel cell types, a DCFC has high system efficiency (~60%) and thus has great potential for GHG reduction. Electric Power Research Institute (EPRI)[3] conducted an assessment of direct coal conversion fuel cells for utility applications and concluded that the technology could be used to address the coal utilization issues with the potential benefits of low carbon pollution, high conversion efficiency, low cost of coal fuel, low cost of concentrated CO_2 sequestration as the by-product, etc. Another huge advantage of DCFC technology is its adaptability to a variety of fuels, such as coal, coke, tar, biomass and organic waste. Fuel utilization in a DCFC can be almost 100% and its product gases are distinct phases and thus can be separated easily.

Based on the electrolytes used, DCFCs can be classified into three categories: molten hydroxide DCFCs, molten carbonate DCFCs and solid oxide DCFCs. Previous R&D of molten hydroxide and molten carbonate DCFCs is reviewed in detail in Refs. 1,2 while solid oxide DCFC development is presented in Ref. 4. The most recent advances in DCFC technology development are summarized in Refs. 4,5, from materials for anodes, cathodes, and electrolytes to system design, carbon fuel morphology, and technical challenges. Despite these recent advances, DCFCs are still in a preliminary development stage. Considerable uncertainties need to be understood and addressed to allow further development, such as reliability, lifetime, cost, etc. Compared to the two other types of DCFCs, molten carbonate DCFCs have been viewed as one of the highly potential types of DCFC systems.[2]

So far most of the DCFC R&D has focused on experimental exploration, which is a costly time consuming process. Modeling simulation, as a powerful complementary tool, can provide insights or guidance on where and how DCFC performance can be improved. However, until now, only limited efforts have been made to develop models due to the complexity of the DCFC system and to incomplete understanding of the CO/CO_2 reversal reaction in the anode. Most available DCFC models are empirical or electrochemical, and do not consider the transport of the gas species within the entire DCFC. For instance, Elleuch et al.[6] developed analytical models for molten carbonate DCFCs and conducted a comparative study for two cases: one producing CO_2 only and one generating a mixture of CO/CO_2. They concluded that under the same operating conditions the DCFC producing a mixture of CO/CO_2 exhibited 15% performance improvement compared to the one producing CO_2 only. Zhang et al.[7] proposed an electrochemical model for fluidized-bed DCFCs and studied the effects of operating conditions (temperature, flow rate, pressures) on performance. Xing et al.[8] proposed an electrochemical model for a molten hydroxide DCFC and investigated how performance varied with temperature, pressure, O_2 flow rate, and fuel mass. Eom et al.[9] modified the electrochemical model by taking into account the correlation function between surface properties and inner resistance. Liu et al.[10] introduced an improved packed bed anode into an electrochemical DCFC model and investigated the effects of temperature, anode dimension, and carbon particle size on cell performance. Li et al.[11] employed a microstructure model of carbon particles to estimate the activity of carbon and to refine the open circuit potential in a DCFC electrochemical model. The above empirical or electrochemical models are very useful in understanding qualitatively the effects of design and operating parameters on DCFC performance. However, these models did not calculate profiles of the reactant species in the DCFC, whose system design and performance therefore could not be fully optimized. Some work has been done to develop comprehensive DCFC models to include gas transport and electrochemical reactions. For example, Alexander et al.[12] developed a 3D model for a solid oxide DCFC. The model was used to calculate the performance of a tubular fuel cell design with idealized electrode exchange current density parameters. Elleuch et al.[13] developed a 2D model for a lab-scale planar DCFC by taking into account the electrochemical mechanism and mass and heat transfer in all regions of the cell. The temperature profile and CO_2 and O_2 concentrations over the cell domain were presented. The effects of temperature, inlet gas flow velocity, porosity of the electrolyte matrix, cathode exchange current density, and anode specific area were discussed. The model did not include the reverse Boudouard reaction. Agarwal[14] investigated the molten carbonate DCFCs using packed bed models and conducted a series of parametric studies. The results demonstrated that the activation and ohmic polarizations were more important to cell performance than the concentration polarization. The model included the transport and electrochemical processes occurring in both the anode and the cathode, but CO generation and axial diffusion were neglected. More recently, Chen and Selman[15,16] developed

[z]E-mail: Zhong.Xie@nrc-cnrc.gc.ca

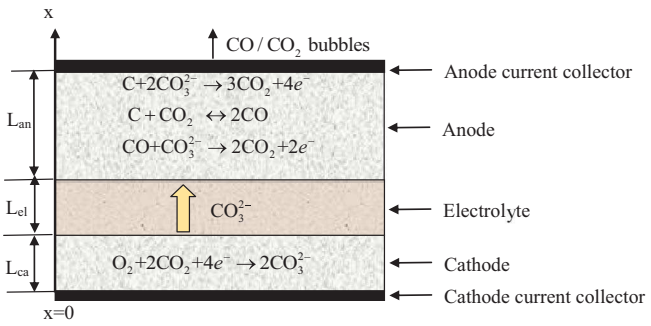

Figure 1. Schematic of a DCFC unit.

a 1D homogenous model for the anode of a molten carbonate DCFC by taking into account both the 4-electron carbon oxidation and the 2-electron CO oxidation reactions as well as the reverse Boudouard reaction. Again it was found that DCFC anode performance is mainly limited by the ohmic losses and the relatively slow anodic reactions. A similar 1D homogenous anode model was employed by Maheshwari et al.[17] to study the dependence of a molten carbonate DCFC's performance on some design and operating parameters, such as bulk conductivities of the solid carbon fuel and the liquid electrolyte in the anode, carbon loading and anode thickness, etc. The anode model[18] was also used to study the dependence of the CO_2 and CO concentration profiles on some operating and electrochemical parameters, such as time, bulk conductivities in the liquid and solid phases, and specific reaction surface area. Such anode models are limited to the anode parameters and cannot be used to study the effects of the cathode- and the electrolyte matrix-related parameters on the DCFC performance.

This paper develops a 1D homogenous unit cell model for a molten carbonate DCFC. The model domain includes all three components of the cell: cathode, anode, and the electrolyte matrix layer between the two electrodes. The 4-electron carbon oxidation reaction, the 2-electron CO oxidation reaction, and the reverse Boudouard reaction are all considered. This unit cell model enables calculation of the potential and the reactant profiles through the thickness of the cell. The model is employed to conduct parametric studies of the effect of volume fractions of the electrode materials, thickness of each component and operating temperature on cell performance.

Model Development

Figure 1 shows a schematic of a whole DCFC unit comprising a cathode, a molten carbonate electrolyte matrix layer, and an anode. O_2 and CO_2 are supplied to the cathode where the following electrochemical reaction occurs:

$$O_2+2CO_2+4e^- \rightarrow 2CO_3^{2-} \quad [1]$$

Carbonate ions generated at the cathode migrate to the anode through the molten carbonate electrolyte matrix via ionic conduction, and react with carbon to produce mostly CO_2 at a relatively low temperature:

$$C + 2CO_3^{2-} \rightarrow 3CO_2+4e^- \quad [2]$$

Experimental studies[19–22] have shown that a mixture of CO/CO_2 exists as the temperature escalates from 600°C to 700°C and higher, which indicate a Boudouard equilibrium reaction and a secondary anodic reaction may take place, as suggested in Ref. 15

$$C + CO_2 \leftrightarrow 2CO \quad [3]$$

and

$$CO + CO_3^{2-} \rightarrow 2CO_2+2e^- \quad [4]$$

The Boudouard equilibrium Reaction 3 is highly dependent on temperature. The forward Boudouard reaction is the CO disproportion reaction of CO → CO_2 and the reverse Boudouard reaction is the reduction of CO_2 → CO which becomes significant when the temperature reaches 700°C.[21]

The overall DCFC reaction is:

$$C+O_2 \rightarrow CO_2 \quad [5]$$

The x-axis direction of the model is from the cathode to the anode and is perpendicular to the molten carbonate matrix layer.

Model Equations

To simplify the model development, the following assumptions apply:

- The system is isothermal.
- Both anode and cathode current collectors are thin and conduct well.
- Gases (CO_2 and O_2) are transported in the gas phase through the pore network of the cathode and dissolve into the electrolyte phase to react.
- The CO/CO_2 mixture produced at the anode bubbles up at a constant velocity.
- The activities of carbon fuel and molten carbonate are unity.
- Electronic and ionic charge balances are based on Ohm's law.
- Butler-Volmer charge transfer kinetics are applied to Reactions 2 and 4.
- Mass balances in the gas phase obey Fick's law.
- Dissolved O_2 and CO_2 in the liquid electrolyte phase obey Henry's law.

Conservation of charge and mass, combined with Ohm's law and Fick's law, yields the following nonlinear model equations:

Gas transport in the cathode.—The cathode of a DCFC unit consists of lithiated NiO and electrolyte (62:38 mol% of Li_2CO_3 and K_2CO_3). Air and CO_2 are supplied to the cathode and are transported in gas phase through the cathode pore network and dissolve into the electrolyte to reach reaction sites where Reaction 1 occurs.

The governing equations for O_2 and CO_2 transport in the cathode can be derived from the mass balance of each species and are given by

$$\frac{d}{dx}\left(-D^{\text{eff}}_{O_2,ca}\frac{d}{dx}\left(\frac{p_{O_2}}{RT}\right)\right) = -\frac{1}{4F}j_{ca} \quad [6]$$

and

$$\frac{d}{dx}\left(-D^{\text{eff}}_{CO_2,ca}\frac{d}{dx}\left(\frac{p_{CO_2,ca}}{RT}\right)\right) = -\frac{1}{2F}j_{ca} \quad [7]$$

where x is the coordinate as shown in Figure 1, $D^{\text{eff}}_{O_2,ca}$ and $D^{\text{eff}}_{CO_2,ca}$ are the effective diffusivities respectively of O_2 and CO_2 in the cathode, the subscript "ca" represents the cathode, p_{O_2} and $p_{CO_2,ca}$ are the respective O_2 and CO_2 gas pressures in the cathode, R is the gas constant, T is cell temperature, F is Faraday's constant, and j_{ca} is the reaction rate in the cathode.

The effective diffusivities of O_2 and CO_2 in Eqs. 6 and 7 are estimated by the Bruggeman equation as

$$D^{\text{eff}}_{O_2,ca} = D_{O_2,ca}\left(\varepsilon_{g,ca}\right)^{1.5} \quad [8]$$

$$D^{\text{eff}}_{CO_2,ca} = D_{CO_2,ca}\left(\varepsilon_{g,ca}\right)^{1.5} \quad [9]$$

here $\varepsilon_{g,ca}$ is the gas porosity of the cathode, $D_{O_2,ca}$ and $D_{CO_2,ca}$ are the diffusivities of O_2 and CO_2 in the gas mixture of O_2, CO_2, and N_2 in the cathode and can be estimated by[23]

$$D_{O_2,ca} = \frac{1-y_{O_2}}{y_{CO_2}/D_{O_2\text{-}CO_2} + y_{N_2}/D_{O_2\text{-}N_2}} \quad [10]$$

and

$$D_{CO_2,ca} = \frac{1-y_{CO_2}}{y_{O_2}/D_{O_2\text{-}CO_2} + y_{N_2}/D_{CO_2\text{-}N_2}} \quad [11]$$

respectively. Here y_{O_2}, y_{CO_2} and y_{N_2} are the respective mole fractions of O_2, CO_2, and N_2, $D_{O_2\text{-}CO_2}$, $D_{O_2\text{-}N_2}$ and $D_{CO_2\text{-}N_2}$ are the respective binary diffusivities of each pair of gas species and given by the Fuller-Schettler-Giddings equation[24]

$$D_{X\text{-}Y} = \frac{10^{-3}T^{1.75}\left(\frac{1}{M_X}+\frac{1}{M_Y}\right)^{1/2}}{p\left[\left(\sum v\right)_X^{1/3}+\left(\sum v\right)_Y^{1/3}\right]^2} \quad [12]$$

where $D_{X\text{-}Y}$ is the binary gas phase diffusivity of species X and Y in cm^2/s, T is cell temperature in Kelvin, p is total cathode pressure in atmospheres, M_X and M_Y are the respective molecular weights of species X and Y in g/mol, $(\sum v)_X$ and $(\sum v)_Y$ are the respective molecular volumes of species X and Y in cm^3/g-mol.

The mole fractions of each gas species in the cathode can be calculated from their partial pressures and the total pressure as

$$y_{O_2} = \frac{p_{O_2}}{p_{tot,ca}};\ y_{CO_2} = \frac{p_{CO_2}}{p_{tot,ca}};\ y_{N_2} = 1 - y_{O_2} - y_{CO_2} \quad [13]$$

The reaction rate in the cathode in Eq. 6 is described by the Butler-Volmer equation[25] as

$$j_{ca} = S_{ca}i^0_{ca}\left[\exp\left(-\alpha_{ca}\frac{n_{ca}F}{RT}\eta_{ca}\right) - \exp\left((1-\alpha_{ca})\frac{n_{ca}F}{RT}\eta_{ca}\right)\right] \quad [14]$$

where S_{ca} is the reaction surface area per volume in the cathode, i^0_{ca} is the exchange current density, α_{ca} is the cathode charge transfer coefficient, η_{ca} is the cathode overpotential, and n_{ca} is the number of electrons in the cathode electrochemical reaction.

Gaseous O_2 and CO_2 must dissolve into the electrolyte phase of the cathode and reach reaction sites to produce carbonate ions. In Eq. 14, the exchange current density is given by[26] as

$$i^0_{ca} = i^0_{0,ca}\left(p^{el}_{CO_2,ca}\right)^{r_1}\left(p^{el}_{O_2,ca}\right)^{r_2} \quad [15]$$

here $i^0_{0,ca}$ is the standard exchange current density, r_1 and r_2 are the cathode reaction parameters, $p^{el}_{CO_2,ca}$ and $p^{el}_{O_2,ca}$ are the respective pressures of the dissolved CO_2 and O_2, and are related to the cathode gas phase pressures by

$$p^{el}_{O_2,ca} = p_{O_2}\left(K_{O_2}RT\right) \quad [16]$$

and

$$p^{el}_{CO_2,ca} = p_{CO_2,ca}\left(K_{CO_2}RT\right) \quad [17]$$

respectively. Here K_{O_2} and K_{CO_2} are the concentration-based solubilities of O_2 and CO_2 respectively in the carbonate electrolyte, and are given by[27]

$$K_{O_2} = K_{0,O_2}\exp\left(-\frac{E_{s,O_2}}{T}\right) \quad [18]$$

and

$$K_{CO_2} = K_{0,CO_2}\exp\left(-\frac{E_{s,CO_2}}{T}\right) \quad [19]$$

respectively. Here K_{0,O_2} and K_{0,CO_2} are reference solubilities of O_2 and CO_2 respectively. E_{s,O_2} and E_{s,CO_2} are two parameters for the solubility calculation.

The overpotential in the cathode is defined as

$$\eta_{ca} = \phi_{so} - \phi_{el} - E_{eq,ca} \quad [20]$$

where ϕ_{so} is the electric potential in the solid phase, ϕ_{el} is the ionic potential in the electrolyte phase, $E_{eq,ca}$ is the equilibrium potential of the cathode, and the subscript "so" and "el" represent the solid and electrolyte phases, respectively.

Gas transport in the anode.—A CO/CO_2 mixture is considered to be the product resulting from the primary and secondary anodic reactions (Eqs. 2 and 4) as well as the Boudouard Reaction 3 in the anode. Theoretically, the gas mixture is transported both as dissolved gases through the liquid electrolyte phase and as gas bubbles through the gas pore network due to buoyancy. Because the movement of the bubbles is more rapid than the net flux of dissolved gases,[15] only the bubble transport is considered and the dissolved gases are assumed to be uniformly distributed in the electrolyte phase of the anode. The governing equations for CO_2 and CO in the anode[15] are

$$\frac{d}{dx}\left(-D^{eff}_{CO_2,an}\frac{d}{dx}\left(\frac{p_{CO_2,an}}{RT}\right)+\frac{p_{CO_2,an}}{RT}v\right) = \frac{3}{4F}j_{an,E2} + \frac{1}{F}j_{an,E4} - j_{Boud} \quad [21]$$

and

$$\frac{d}{dx}\left(-D^{eff}_{CO,an}\frac{d}{dx}\left(\frac{p_{CO}}{RT}\right)+\frac{p_{CO}}{RT}v\right) = -\frac{1}{2F}j_{an,E4} + 2j_{Boud} \quad [22]$$

Here $D^{eff}_{CO_2,an}$ and $D^{eff}_{CO,an}$ are the effective diffusivities of CO_2 and CO in the anode respectively, the subscript "an" represents the anode, $p_{CO_2,an}$ and p_{CO} are the CO_2 and CO gas pressures respectively in the anode, v is the velocity of the gas bubbles, $j_{an,E2}$ and $j_{an,E4}$ are the reaction rates of electrochemical Reactions 2 and 4 respectively, and j_{Boud} is the reaction rate of the reverse Boudouard Reaction 3.

The effective diffusivities of CO_2 and CO in the anode can be calculated from the porosity of the anode, based on the Bruggeman equation, as

$$D^{eff}_{CO_2,an} = D_{CO_2-CO}\left(\varepsilon_{g,an}\right)^{1.5} \quad [23]$$

and

$$D^{eff}_{CO,an} = D_{CO_2-CO}\left(\varepsilon_{g,an}\right)^{1.5} \quad [24]$$

Here $\varepsilon_{g,an}$ is the gas porosity of the anode, D_{CO_2-CO} is the binary diffusivity of CO_2 or CO in the gas mixture of the anode and can be obtained from Eq. 12.

The reaction rates for the primary and secondary anodic electrochemical reactions (Eqs. 2 and 4, respectively) in Eqs. 21 and 22 are given by the Butler-Volmer equation[15] as

$$j_{an,E2} = S_{an,E2}i^0_{an,E2}\left[\exp\left(\alpha_{an,E2}\frac{n_{an,E2}F}{RT}\eta_{an,E2}\right) - \exp\left(-\left(1-\alpha_{an,E2}\right)\frac{n_{an,E2}F}{RT}\eta_{an,E2}\right)\right] \quad [25]$$

and

$$j_{an,E4} = S_{an,E4}i^0_{an,E4}\left[\exp\left(\alpha_{an,E4}\frac{n_{an,E4}F}{RT}\eta_{an,E4}\right) - \exp\left(-\left(1-\alpha_{an,E4}\right)\frac{n_{an,E4}F}{RT}\eta_{an,E4}\right)\right] \quad [26]$$

where $S_{an,E2}$ and $S_{an,E4}$ are the reaction surface areas per unit volume in the anode for electrochemical Reactions 2 and 4 respectively, $i^0_{an,E2}$ and $i^0_{an,E4}$ are the anode exchange current densities respectively for the two reactions, $\alpha_{an,E2}$ and $\alpha_{an,E4}$ are the respective anode transfer coefficients, $n_{an,E2}$ and $n_{an,E4}$ are the numbers of electrons in the two anodic electrochemical reactions respectively, and $\eta_{an,E2}$ and $\eta_{an,E4}$ are the overpotentials corresponding to the two reactions and are defined as

$$\eta_{an,E2} = \phi_{so} - \phi_{el} - E_{eq,an,E2} \quad [27]$$

and

$$\eta_{an,E4} = \phi_{so} - \phi_{el} - E_{eq,an,E4} \quad [28]$$

where $E_{eq,an,E2}$ and $E_{eq,an,E4}$ are the equilibrium potentials of Reactions 2 and 4, respectively.

Assuming the equilibrium potentials in the anode reactions are zero,

$$E_{eq,an,E2} = 0, \quad E_{eq,an,E4} = 0 \quad [29]$$

then the equilibrium potential in the cathode equals the open circuit voltage of the cell

$$E_{\mathrm{eq,ca}} = V_{\mathrm{OCV}} \quad [30]$$

where V_{OCV} is the open circuit voltage of the cell.

The temperature dependence of the anode exchange current density in Eq. 25 for the primary anodic electrochemical Reaction 2 is given by[6]

$$i^0_{\mathrm{an,E2}} = K_{\mathrm{B}} \exp\left(-\frac{E_{\mathrm{B}}}{T}\right) \quad [31]$$

where K_{B} and E_{B} are the pre-exponential factor and the temperature activation of the Reaction 2.

The reaction rate of the reverse Boudouard Reaction 3 in Eqs. 21 and 22, j_{Boud}, is expressed by[15]

$$j_{\mathrm{Boud}} = K_{\mathrm{Boud}} W_{\mathrm{C}} \left(p_{\mathrm{CO_2,an}} - p_{\mathrm{CO_2,Boud}}\right) \quad [32]$$

where K_{Boud} is the rate constant, W_{C} is the mass concentration of carbon, $p_{\mathrm{CO_2,Boud}}$ is the partial pressure of CO_2 at Boudouard equilibrium.

The mass concentration of carbon in the anode is estimated by

$$W_{\mathrm{C}} = \varepsilon_{\mathrm{so,an}} \rho_{\mathrm{C}} \quad [33]$$

where $\varepsilon_{\mathrm{so,an}}$ and ρ_{C} are the volume fraction and density of carbon in the anode.

The partial pressure of CO_2 at Boudouard equilibrium depends on the total pressure of the gas mixture of CO_2/CO and on temperature, and can be estimated as follows:

The equilibrium constant of the Boudouard reaction is defined by the partial pressures of CO and CO_2[21] as

$$K_{\mathrm{p}} = \frac{\left(p_{\mathrm{CO,Boud}}\right)^2}{p_{\mathrm{CO_2,Boud}} a_{\mathrm{C}}} = \frac{\left(p_{\mathrm{tot,an}} - p_{\mathrm{CO_2,Boud}}\right)^2}{p_{\mathrm{CO_2,Boud}} a_{\mathrm{C}}} \quad [34]$$

where $p_{\mathrm{tot,an}} = p_{\mathrm{CO,Boud}} + p_{\mathrm{CO_2,Boud}}$ is the total pressure of the anode, $a_{\mathrm{C}} = 1$ is the activity of solid carbon fuel, $p_{\mathrm{CO,Boud}}$ and $p_{\mathrm{CO_2,Boud}}$ are the partial pressures of CO and CO_2 at Boudouard equilibrium, respectively.

$p_{\mathrm{CO_2,Boud}}$ can be solved from Eq. 34 as

$$p_{\mathrm{CO_2,Boud}} = \left(\frac{K_{\mathrm{p}}}{2} + p_{\mathrm{tot,an}}\right) - \sqrt{\left(\frac{K_{\mathrm{p}}}{2} + p_{\mathrm{tot,an}}\right)^2 - \left(p_{\mathrm{tot,an}}\right)^2} \quad [35]$$

The equilibrium constant is estimated using the Gibbs free energy of the Boudouard reaction

$$\Delta G = \left(\Delta H_{\mathrm{CO}} - T\Delta S_{\mathrm{CO}}\right) - \left(\Delta H_{\mathrm{CO_2}} - T\Delta S_{\mathrm{CO_2}}\right) = -RT \ln\left(\frac{K_{\mathrm{p}}}{p_{\mathrm{tot,an}}}\right) \quad [36]$$

where ΔG is the Gibbs free energy, ΔH_{CO} and $\Delta H_{\mathrm{CO_2}}$ are the corresponding enthalpies, ΔS_{CO} and $\Delta S_{\mathrm{CO_2}}$ are the corresponding entropies.

Electronic charge transport in both cathode and anode.—Electronic charge transport in the cathode and the anode obey Ohm's law and the governing equations are

$$\text{In the cathode:} \quad \frac{d}{dx}\left(-\sigma^{\mathrm{eff}}_{\mathrm{so,ca}} \frac{d}{dx}\phi_{\mathrm{so,ca}}\right) = j_{\mathrm{ca}} \quad [37]$$

$$\text{In the anode:} \quad \frac{d}{dx}\left(-\sigma^{\mathrm{eff}}_{\mathrm{so,an}} \frac{d}{dx}\phi_{\mathrm{so,an}}\right) = -\left(j_{\mathrm{an,E2}} + j_{\mathrm{an,E4}}\right) \quad [38]$$

where $\phi_{\mathrm{so,ca}}$ and $\phi_{\mathrm{so,an}}$ are the respective electric potentials in the cathode and anode, $\sigma^{\mathrm{eff}}_{\mathrm{so,ca}}$ and $\sigma^{\mathrm{eff}}_{\mathrm{so,an}}$ are the respective effective electric conductivities in the cathode and anode.

The insufficient electrical connectivity among the lithiated NiO agglomerates in the cathode and the carbon particles in the anode might make the effective electronic conductivities of the cathode and the anode much less than their bulk values. Similar to the Bruggeman equation, it is assumed here that the effective electronic conductivity of the cathode or the anode depends on the volume fraction of the corresponding solid material as expressed by an exponential relationship

$$\sigma^{\mathrm{eff}}_{\mathrm{so,ca}} = \sigma_{\mathrm{LiNiO}} \left(\varepsilon_{\mathrm{so,ca}}\right)^{d_{\mathrm{so,ca}}} \quad [39]$$

and

$$\sigma^{\mathrm{eff}}_{\mathrm{so,an}} = \sigma_{\mathrm{C}} \left(\varepsilon_{\mathrm{so,an}}\right)^{d_{\mathrm{so,an}}} \quad [40]$$

where σ_{LiNiO} and σ_{C} are the bulk electric conductivities of lithiated NiO in the cathode and carbon particles respectively in the anode, $\varepsilon_{\mathrm{so,ca}}$ and $\varepsilon_{\mathrm{so,an}}$ are the solid phase volume fractions respectively in cathode and anode, and $d_{\mathrm{so,ca}}$ and $d_{\mathrm{so,an}}$ are the adjusting exponential parameters.

Ionic charge transport in the cell.—Ionic charge transport in the unit cell also obeys Ohm's law and the governing equations are

$$\begin{cases} \frac{d}{dx}\left(-\sigma^{\mathrm{eff}}_{\mathrm{el,ca}} \frac{d}{dx}\phi_{\mathrm{el}}\right) = -j_{\mathrm{ca}}, & \text{in the cathode electrode} \\ \frac{d}{dx}\left(-\sigma^{\mathrm{eff}}_{\mathrm{el}} \frac{d}{dx}\phi_{\mathrm{el}}\right) = 0, & \text{in the electrolyte layer} \\ \frac{d}{dx}\left(-\sigma^{\mathrm{eff}}_{\mathrm{el,an}} \frac{d}{dx}\phi_{\mathrm{el}}\right) = j_{\mathrm{an,E2}} + j_{\mathrm{an,E4}}, & \text{in the anode electrode} \end{cases} \quad [41]$$

where ϕ_{el} is the ionic potential, $\sigma^{\mathrm{eff}}_{\mathrm{el,ca}}$, $\sigma^{\mathrm{eff}}_{\mathrm{el}}$ and $\sigma^{\mathrm{eff}}_{\mathrm{el,an}}$ are the effective ionic conductivities in the cathode, the electrolyte matrix, and the anode, respectively, and are estimated from the following exponential equations,

$$\sigma^{\mathrm{eff}}_{\mathrm{el,ca}} = \sigma_{\mathrm{el}} \left(1 - \varepsilon_{\mathrm{g,ca}} - \varepsilon_{\mathrm{so,ca}}\right)^{d_{\mathrm{el}}} \quad [42]$$

$$\sigma^{\mathrm{eff}}_{\mathrm{el}} = \sigma_{\mathrm{el}} \left(\varepsilon_{\mathrm{l,el}}\right)^{d_{\mathrm{el}}} \quad [43]$$

$$\sigma^{\mathrm{eff}}_{\mathrm{el,an}} = \sigma_{\mathrm{el}} \left(1 - \varepsilon_{\mathrm{g,an}} - \varepsilon_{\mathrm{so,an}}\right)^{d_{\mathrm{el}}} \quad [44]$$

Here $\varepsilon_{\mathrm{l,el}}$ is the liquid porosity of the electrolyte layer matrix, d_{el} is a adjusting exponential parameter indicating the dependence of the effective conductivity of the electrolyte on its volume fraction in each component in the DCFC unit. The bulk ionic conductivity, σ_{el} in the carbonate electrolyte with a composition 62:38 mol% of Li_2CO_3 and K_2CO_3 is given by[28]

$$\sigma_{\mathrm{el}} = \sigma^0_{\mathrm{el}} \exp\left(-\frac{E_{\mathrm{el}}}{RT}\right) \quad [45]$$

Boundary Conditions

For the O_2 pressure in the cathode

- Specified O_2 pressure at the cathode outside boundary: $p_{\mathrm{O_2}}|_{x=0} = p^0_{\mathrm{O_2,ca}}$
- Zero O_2 flux at the interface of the cathode and the electrolyte matrix layer: $[-D^{\mathrm{eff}}_{\mathrm{O_2,ca}} \frac{d}{dx}(\frac{p_{\mathrm{O_2}}}{RT})]|_{x=L_{\mathrm{ca}}} = 0$

For the CO_2 pressure in the cathode

- Specified CO_2 pressure at the cathode outside boundary: $p_{\mathrm{CO_2,ca}}|_{x=0} = p^0_{\mathrm{CO_2,ca}}$
- Zero CO_2 flux at the interface of the cathode and the electrolyte matrix layer: $[-D^{\mathrm{eff}}_{\mathrm{CO_2,ca}} \frac{d}{dx}(\frac{p_{\mathrm{CO_2,ca}}}{RT})]|_{x=L_{\mathrm{ca}}} = 0$

For the CO_2 pressure in the anode

- Specified CO_2 pressure at the anode outside boundary: $p_{\mathrm{CO_2,an}}|_{x=L_{\mathrm{ca}}+L_{\mathrm{el}}+L_{\mathrm{an}}} = p^0_{\mathrm{CO_2,an}}$
- Zero CO_2 diffusion flux at the anode outside boundary: $[-D^{\mathrm{eff}}_{\mathrm{CO_2,an}} \frac{d}{dx}(\frac{p_{\mathrm{CO_2,an}}}{RT})]|_{x=L_{\mathrm{ca}}+L_{\mathrm{el}}+L_{\mathrm{an}}} = 0$

For the CO pressure in the anode

- Specified CO pressure at the anode outside boundary: $p_{\mathrm{CO}}|_{x=L_{\mathrm{ca}}+L_{\mathrm{el}}+L_{\mathrm{an}}} = p^0_{\mathrm{CO,an}}$
- Zero CO diffusion flux at the anode outside boundary: $[-D^{\mathrm{eff}}_{\mathrm{CO,an}} \frac{d}{dx}(\frac{p_{\mathrm{CO}}}{RT})]|_{x=L_{\mathrm{ca}}+L_{\mathrm{el}}+L_{\mathrm{an}}} = 0$

For the electric potential in the anode

- Electrical ground condition at the anode outside boundary: $\phi_{so,an}|_{x=L_{ca}+L_{el}+L_{an}} = 0$
- Zero electric current density at the interface of the anode and the electrolyte matrix layer: $(-\sigma^{eff}_{so,an}\frac{d}{dx}\phi_{so,an})|_{x=L_{ca}+L_{el}} = 0$

For the electric potential in the cathode

- Zero electrical current at the interface of the electrolyte matrix layer and the cathode: $(-\sigma^{eff}_{so,ca}\frac{d}{dx}\phi_{so,ca})|_{x=L_{ca}} = 0$
- Specified cell voltage at the cathode outside boundary: $\phi_{so}|_{x=0} = V_{cell}$

For the ionic potential in the unit cell

- Zero ionic current density at the anode outside boundary: $(-\sigma^{eff}_{el,an}\frac{d}{dx}\phi_{el})|_{x=L_{ca}+L_{el}+L_{an}} = 0$
- Zero ionic current density at the cathode outside boundary: $(-\sigma^{eff}_{el,ca}\frac{d}{dx}\phi_{el})|_{x=0} = 0$

Polarization curve.—The cell current density can be estimated at the cathode outside boundary as

$$i_{cell} = -\left(-\sigma^{eff}_{so,ca}\frac{d}{dx}\phi_{so,ca}\right)\Big|_{x=0} \quad [46]$$

For specified cell voltages, $V_{cell} = [V_{OCV}, V_{OCV} - 0.1, V_{OCV} - 0.2, \ldots, 0]$, the cell current density can be calculated using Eq. 46. Then (i_{cell}, V_{cell}) generates the polarization curve.

Simulation Results and Discussions

Input parameters and model validation.—The model is coded and solved by using the MATLAB software. There is not much information available about the model parameter values for DCFCs. Therefore in this work most of the model parameter values are adopted from molten carbon fuel cells due to the two fuel cells having similar cathodes. The model input parameters are listed in Table I.

The thickness of each component of the unit cell, namely, cathode, electrolyte matrix layer, and anode, is estimated using the cell material composition and the total cell thickness of 1 mm from Ref. 29. The effective conductivities in both solid phase and electrolyte phase depend highly on particle size, electrode structure, and volume fractions of solid and electrolyte materials. We were not able to fit the testing data by applying the Bruggeman equation (with the exponential correction factor equal to 1.5) to the effective conductivities of electrolyte and solid phases. As pointed out in Refs. 30,33, the estimation of the actual effective conductivities of electrolyte and solid phases in porous electrodes is difficult and past modeling work has often suggested using the exponential correction factors, $d_{so,an}$, $d_{so,ca}$ and d_{el}, as fitting parameters. In addition, a reaction surface area of 2700 cm^2/cm^3 is used in Ref. 25 for the anode of a molten carbonate fuel cell. Due to weak connection between carbon particles, the real reaction surface area in the anode of a DCFC might be smaller than that of the anode of a MCFC. Therefore, $S_{an,E2} = S_{an,E4} = 2000$ cm^2/cm^3 is applied in this work for the anode reaction surface area in the simulation. The calculated polarization curve from modeling simulation is compared with the testing data in Figure 2.

The fitted values for $d_{so,an}$, $d_{so,ca}$ and d_{el} are 9.0, 1.5 and 2.5, respectively, and the corresponding effective conductivities in the anode, the cathode, and the electrolyte matrix are: $\sigma^{eff}_{so,an} = 0.251$ S/cm, $\sigma^{eff}_{so,ca} = 6.244$ S/cm, $\sigma^{eff}_{el,an} = 0.0082$ S/cm, $\sigma^{eff}_{el,ca} = 0.046$ S/cm, and $\sigma^{eff}_{el} = 0.384$ S/cm. These low effective conductivities in the anode indicate that, besides the slow anodic reactions, the cell performance is mainly limited by the ohmic losses from the solid and electrolyte phases of the anode.

The partial pressures of gas species in both cathode and anode at a current density of 0.2 A/cm^2 are presented in Figure 3. In the cathode, CO_2 and O_2 are consumed so their partial pressures decrease through the cathode from outside to inside. Figures 3a and 3b shows

Table I. DCFC model input parameters.

Parameter	Value	Source
L_{ca}	0.017 cm	estimated from Ref. 29
L_{el}	0.045 cm	estimated from Ref. 29
L_{an}	0.038 cm	estimated from Ref. 29
$\varepsilon_{g,an}$	0.4	estimated from Ref. 29
$\varepsilon_{so,an}$	0.45	estimated from Ref. 29
$\varepsilon_{g,ca}$	0.4	30
$\varepsilon_{so,ca}$	0.3	30
$\varepsilon_{l,el}$	0.7	30
T	923 K	
ΔH_{CO}	−232.7 kJ/mol	31
ΔS_{CO}	0.1679 kJ/(mol K)	31
ΔH_{CO_2}	−395.6 kJ/mol	31
ΔS_{CO_2}	0 kJ/(mol K)	31
$p^0_{tot,an}$	1 atm	
$p^0_{CO_2,an}$	0.7925 atm	15,16
$p^0_{CO,an}$	0.2075 atm	15,16
$p^0_{tot,ca}$	1 atm	
$p^0_{CO_2,ca}$	0.3 atm	
$p^0_{O_2,ca}$	$0.21 \times (p^0_{tot,ca} - p^0_{CO_2,ca})$ atm	
F	96485 C/mol	
R	8.315 J/(mol K)	
V_{OCV}	0.931 V	29
M_{O_2}	32 g/mol	
M_{N_2}	28 g/mol	
M_{CO_2}	44 g/mol	
M_{CO}	28 g/mol	
$(\sum \nu)_{O_2}$	16.6 cm^3	
$(\sum \nu)_{N_2}$	17.9 cm^3	
$(\sum \nu)_{CO_2}$	26.9 cm^3	
$(\sum \nu)_{CO}$	18.9 cm^3	
K_B	5.8×10^5 A/cm^2	6
E_B	22175 K	6
$\alpha_{an,E2}$	0.5	15
$\alpha_{an,E4}$	0.5	15
$S_{an,E2}$	2000 cm^2/cm^3	fitting
$S_{an,E4}$	2000 cm^2/cm^3	fitting
$i^0_{an,E4}$	8.2×10^{-5} A/cm^2	15
α_{ca}	0.5	6
n_{ca}	4	
$E_{eq,ca}$	V_{OCV} V	
$E_{eq,an,E2}$	0 V	
$E_{eq,an,E4}$	0 V	
$n_{an,E2}$	4	
$n_{an,E4}$	2	
v	1 cm/s	15
S_{ca}	3000 cm^2/cm^3	25
$i^0_{0,ca}$	1.01×10^{-3} A/cm^2	25
K_{Boud}	4×10^{-7} mol/(g atm s)	15
ρ_C	2.134 g/cm^3	29
E_{s,O_2}	7589 K	27
K_{0,O_2}	$e^{9.592} \times 10^{-7}$ mol/(cm^3atm)	27
r_1	−1.25	26
r_2	0.375	26
σ_C	331.7 S/cm	6
σ_{LiNiO}	38.0 S/cm	32
d_{el}	2.5	fitting
$d_{so,an}$	9.0	fitting
$d_{so,ca}$	1.5	Bruggeman equation
E_{s,CO_2}	364.6 K	27
K_{0,CO_2}	$e^{5.154} \times 10^{-7}$ mol/(cm^3atm)	27
E_{el}	21910 J/mol	28
σ^0_{el}	23.22 S/cm	28

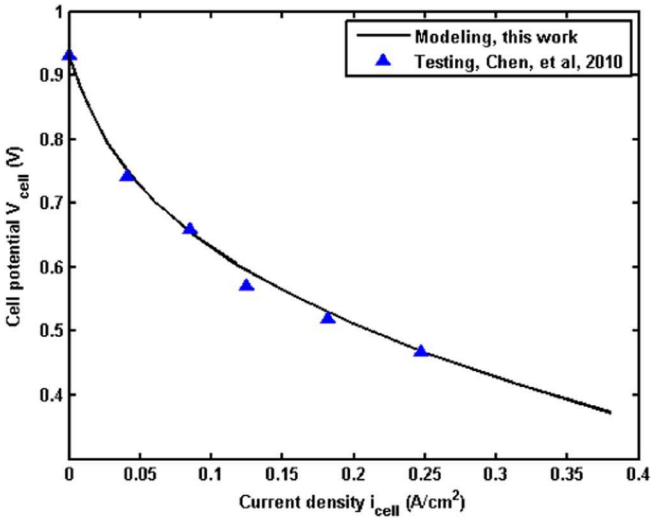

Figure 2. Comparison of polarization curves of a DCFC cell.

that the partial pressure drops of CO_2 and O_2 in the cathode due to cathode reaction consumption are negligible, indicating that here the gas transport in the cathode is not the limiting factor for DCFC performance. This differs from the commercial hydrogen fuel cells, for example, proton exchange membrane fuel cells, where Oxygen transport through the cathode electrode is one of the determining factors for fuel cell performance.[34] On the other hand, the partial pressure of CO_2 in the anode increases from the inside to the specified value of 0.9275 atm at the outside of the anode, implying that near the inside of the anode more CO_2 is converted into CO by the reverse Boudouard Reaction 3, as shown in Figure 3c. Accordingly, the partial pressure of CO decreases from a higher value near the inside of the anode to the specified value of 0.2075 atm at the outside of the anode, as shown in Figure 3d. Note that the constant concentration levels of 0.7925 atm for CO_2 and 0.21075 atm for CO near the outside of the anode, as observed in Refs. 15,18, did not occur here because a much thinner anode was used (0.038 cm vs. 3.8 cm). It was found that at a current density of 0.2 A/cm^2 the diffusion flux of CO_2 in the anode was of the order of 10^{-7} mol s^{-1} cm^{-2} while its convection flux was of the order of 10^{-5} mol s^{-1} cm^{-2}. For CO, its diffusion flux was of the order of -10^{-8} mol s^{-1} cm^{-2} and its convection flux was of the order of 10^{-6} mol s^{-1} cm^{-2}. Therefore, convection caused by bubble movement from the inside to the outside of the anode is the dominant mechanism for both CO_2 and CO transport.

The electric potentials in both the cathode and the anode, and the ionic potential through the electrolyte phase of the unit cell at the same current density of 0.2 A/cm^2, are plotted in Figure 4. Note that the electric potential drop in the anode is 27 mV while the drop in the cathode is negligible. This suggests that reducing the omhic loss in the anode, for example, by reducing its thickness via loading less carbon, may improve cell performance. The increase of the ionic potential in the electrolyte phase of the anode (214 mV) is much larger than the increase in the cathode (39 mV), implying that cell performance is more

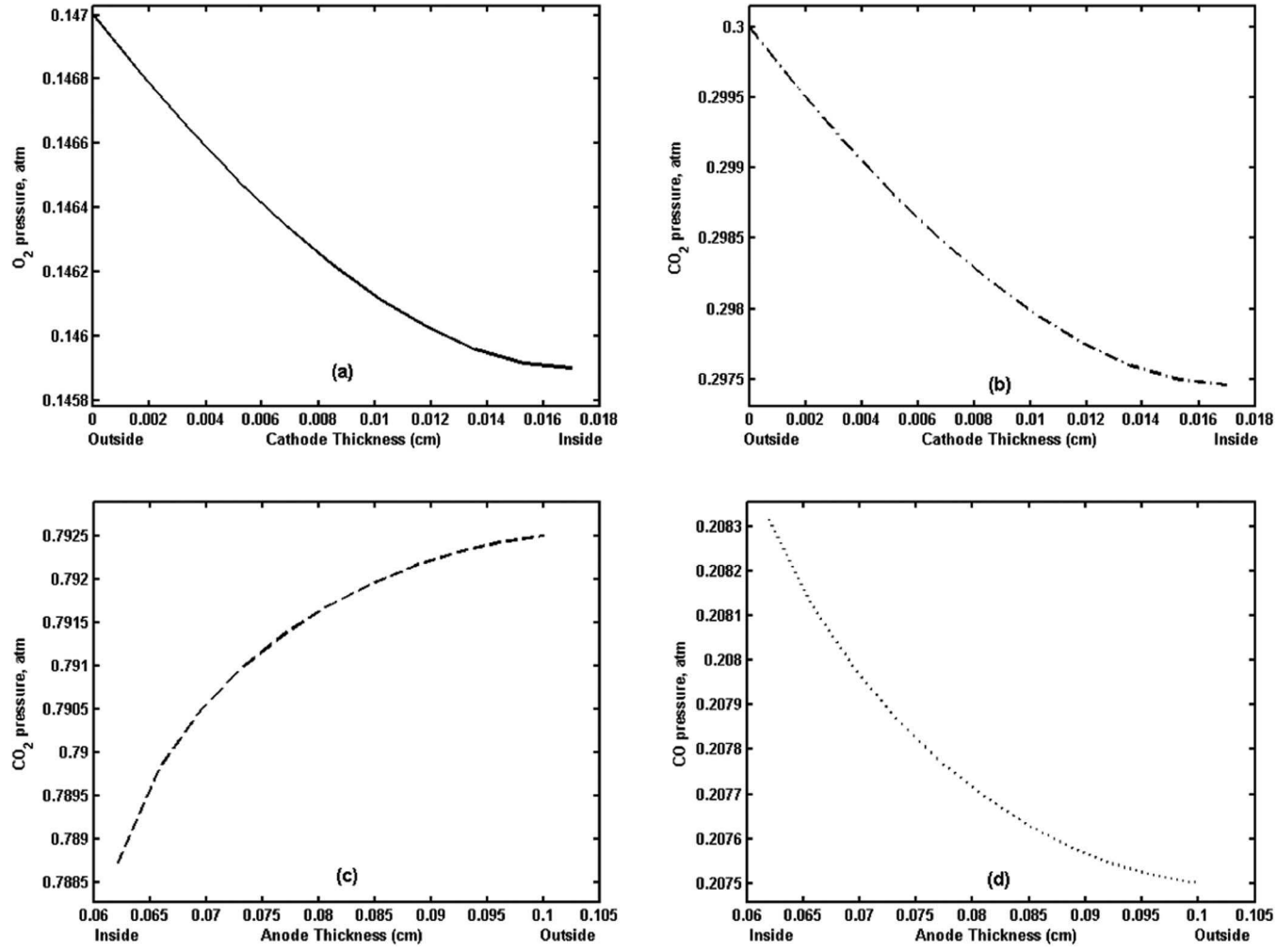

Figure 3. Distributions of gas partial pressures at $i_{cell} = 0.2$ A/cm^2. (a) Cathode O_2; (b) Cathode CO_2; (c) Anode CO_2; (d) Anode CO.

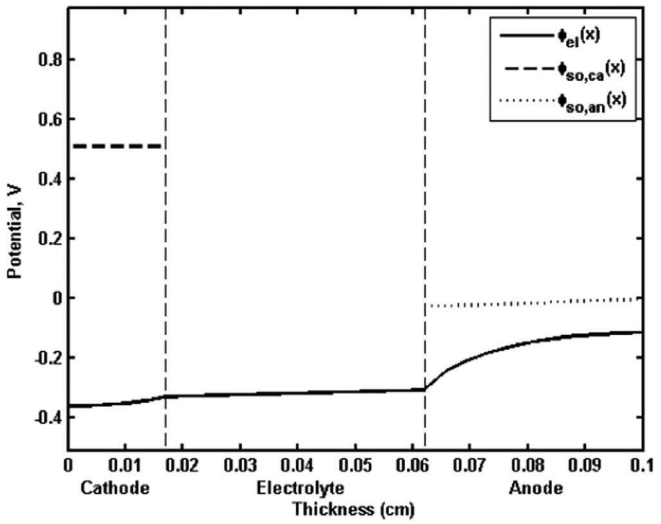

Figure 4. Potential distributions in the DCFC unit at $i_{cell} = 0.2$ A/cm^2.

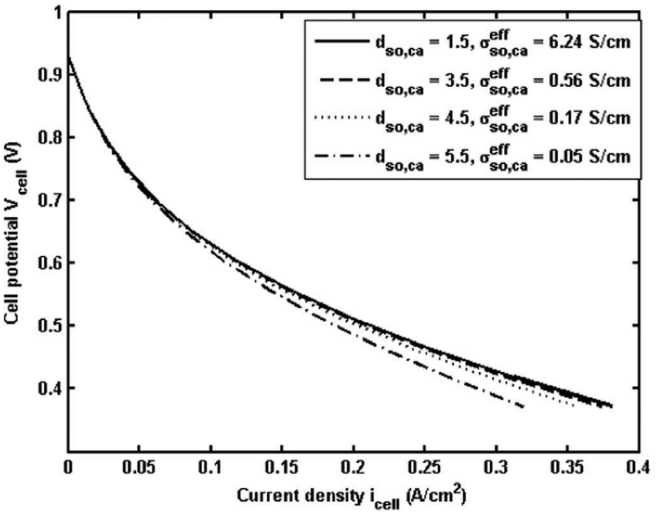

Figure 5. Performance variation with the effective electronic conductivity of the cathode.

sensitive to the effective conductivity of the electrolyte phase in the anode than in the cathode. Thus, adding more electrolyte carbonates into the anode, to assure a high effective ionic conductivity, could enhance the DCFC performance, as observed in Ref. 29. However, there is a balance between the carbon fuel and the electrolyte carbonates in the anode. This will be discussed in the next section.

Effect of cathode effective electronic conductivity.—Figure 5 plots the variation of DCFC performance against the effective electronic conductivity of the cathode solid material where all the parameters are fixed except the exponential factor $d_{so,ca}$. The results show that when the effective electronic conductivity of the cathode drops from 6.24 S/cm ($d_{so,ca} = 1.5$) to 0.56 S/cm ($d_{so,ca} = 3.5$), DCFC performance hardly changes. These results suggest that it is feasible to develop a new cathode material for DCFCs with lower effective electronic conductivity (>0.56 S/cm) to replace the pure lithiated NiO cathode, without sacrificing performance. For example, a set of binary- or ternary-systems of LiFeO2, NiO and LiCoO2, has been investigated as alternative cathode materials for MCFCs, with the measured effective electronic conductivity of the cathode varying from 0.027 to 0.86 S/cm, as demonstrated in Ref. 35.

Effect of electrode material volume fraction.—It is important to balance the electronic conductivity and ionic conductivity in a porous electrode, especially for the DCFC anode where the carbon fuel and the liquid electrolyte contact the current collector and the reaction gas product is transported out of the cell. In this study the gas porosity of each electrode is fixed as given in Table I. The effects of cathode and anode material volume fractions on cell performance are presented in Figure 6 and Figure 7, respectively. Increasing the volume fraction of the solid material of each electrode will improve the effective electric conductivity of the solid phase. At the same time, this decreases the volume fraction of electrolyte phase, which reduces the effective ionic conductivity. Figure 6a simulates the cell performances of three volume fractions of lithiated NiO in the cathode using $d_{so,ca} = 1.5$. When the volume fraction of the lithiated NiO in the cathode increases from 0.1 to 0.3, and 0.5, the corresponding cathode effective electronic conductivities increase from 1.20 to 6.24, and 13.44 S/cm, respectively, while the corresponding cathode effective ionic conductivities decrease from 1.65×10^{-1} to 4.61×10^{-2} and 2.96×10^{-3} S/cm respectively. The corresponding cell performances always decrease because the performance loss from the increase in ionic resistance of the liquid electrolyte phase of the cathode always exceeds the gain from the decrease in ohmic resistance of the solid phase of the cathode. However, when $d_{so,ca} = 3.5$, simulation results demonstrate that optimal volume fractions exist for the solid material and the liquid electrolyte in the cathode, as shown in Figure 6b. When $\varepsilon_{so,ca}$ increases from 0.1 to 0.3,

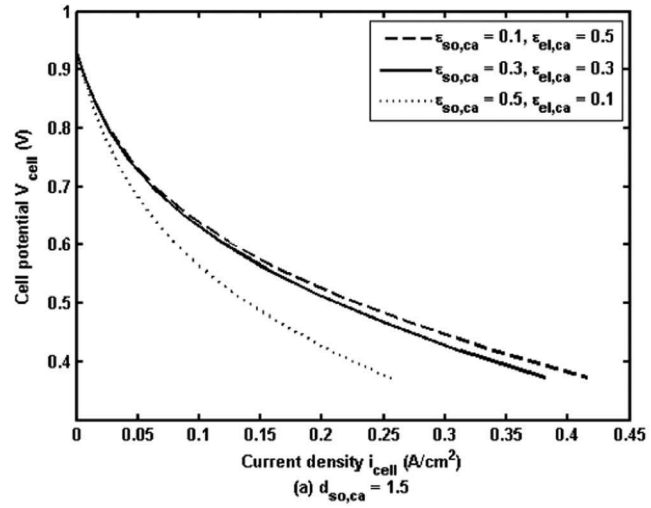

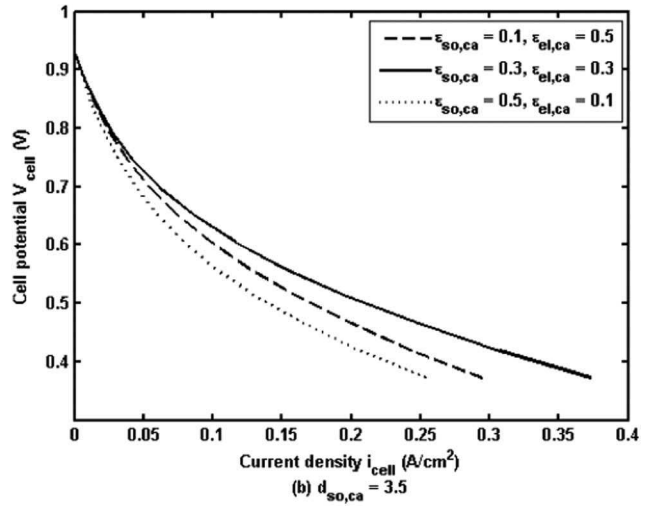

Figure 6. Effect of cathode material volume fraction on DCFC performance.

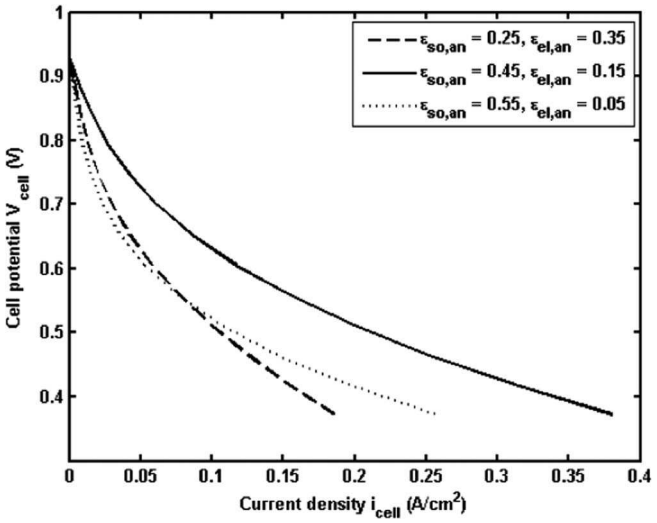

Figure 7. Effect of anode material volume fraction on DCFC performance.

the corresponding effective conductivity of the solid phase increases from 1.20×10^{-2} to 5.62×10^{-1}S/cm. Cell performance is improved from the dashed line to the solid line. With a further increase from 0.3 to 0.5, the corresponding effective conductivity of the solid phase increases from 5.62×10^{-1} to 3.36 S/cm, but performance drops from the solid line to the dotted line. This indicates that the optimal volume fraction of lithiated NiO in the cathode lies between 0.1 and 0.5 for the given parameter values. Further calculation shows that the optimal volume fractions of lithiated NiO and the liquid electrolyte in the cathode are 0.23 and 0.37, respectively, with corresponding effective electronic conductivity and effective ionic conductivity of 2.22×10^{-1} and 7.79×10^{-2} S/cm, respectively.

For the anode, when the volume fraction of carbon increases from 0.25 to 0.45, DCFC performance improves from the dashed line to the solid line in Figure 7. With a further increase from 0.45 to 0.55, the performance drops again from the solid line to the dotted line. This means the optimal volume fraction of carbon in the anode lies between 0.25 and 0.55. More simulations give the optimal volume factions of the carbon and liquid electrolyte in the anode at 0.45 and 0.15, respectively, and the corresponding effective electronic conductivity and effectively ionic conductivity are 2.51×10^{-1} and 8.15×10^{-3} S/cm.

Effect of electrode and electrolyte matrix thicknesses.—The variation of DCFC performance with thickness of the cathode, the electrolyte matrix layer, and thickness of the anode are plotted in Figure 8, Figure 9, and Figure 10, respectively.

As mentioned above, for the cathode of this DCFC, the gas transport and ohmic losses are not the limiting factors. When the cathode thickness increased from 0.007 cm to 0.017 cm, DCFC performance improves noticeably, as shown in Figure 8a, because a thicker cath-

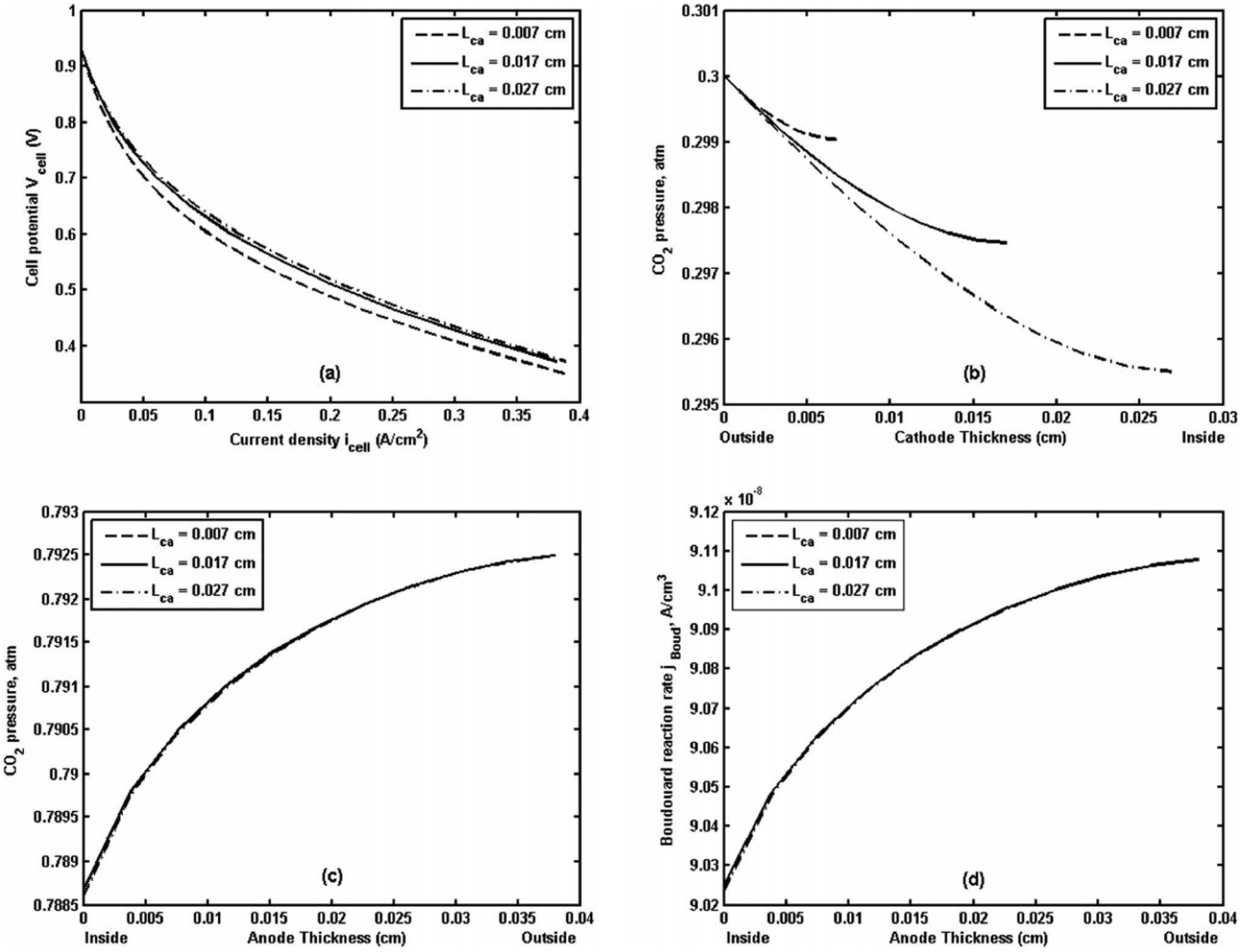

Figure 8. Effect of cathode thickness. (a) DCFC performance; (b) Cathode CO_2 distribution at $I_{cell} = 0.2$ A cm^{-2}; (c) Anode CO_2 distribution at $I_{cell} = 0.2$ A cm^{-2}; (d) Anode Boudouard reaction rate distribution at $I_{cell} = 0.2$ A cm^{-2}.

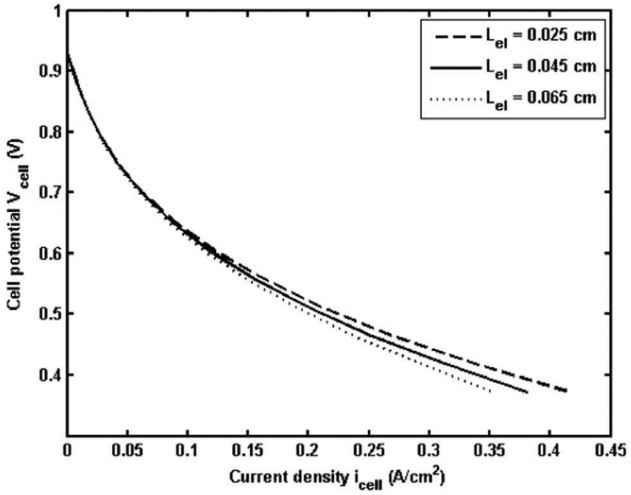

Figure 9. Effect of electrolyte matrix thickness on DCFC performance.

ode provides a thicker zone for the cathode reaction. However, upon further increases from 0.017 cm to 0.027 cm and beyond, the performance improvement is marginal due to a limited reaction zone increase.

The changes of CO_2 distribution in the cathode and anode, and the Boudouard reaction rate distribution in the anode with cathode thickness at the cell current density of 0.2 Acm^{-2} are plotted in Figures 8b, 8c and 8d, respectively. A thicker cathode leads to a lower CO_2 distribution due to increased diffusion resistance in the cathode, as shown in Figure 8b, while the CO_2 distribution in the anode remains almost constant for the three cathode thicknesses due to the same amount of CO_2 is needed in the same anode to achieve the same output of current density (0.2 Acm^{-2}) as shown in Figure 8c. Similarly, Figure 8d shows that the distribution of the Boudouard reaction rate at the current density of 0.2 Acm^{-2}, defined by Eq. 32, remains almost unchanged due to its dependence on CO_2 distribution in the anode.

For the electrolyte matrix, an increase in thickness corresponds to a bigger ohmic loss, and therefore decreases DCFC performance, especially for large current densities, as shown in Figure 9.

Figure 10a shows the effects of the anode thickness on cell performance. When anode thickness increases from 0.018 cm to 0.058 cm, cell performance improves for small current densities (anode kinetics control range) but then decreases for large current densities (both anode kinetics and ohmic control range). This indicates that a thicker anode will improve anode kinetics while ohmic loss will dominate DCFC performance at large current densities.

The effect of anode thickness on CO_2 distribution in the cathode and anode, and on the Boudouard reaction rate distribution in the anode at the cell current density of 0.2 Acm^{-2} are plotted in Figures 10b, 10c

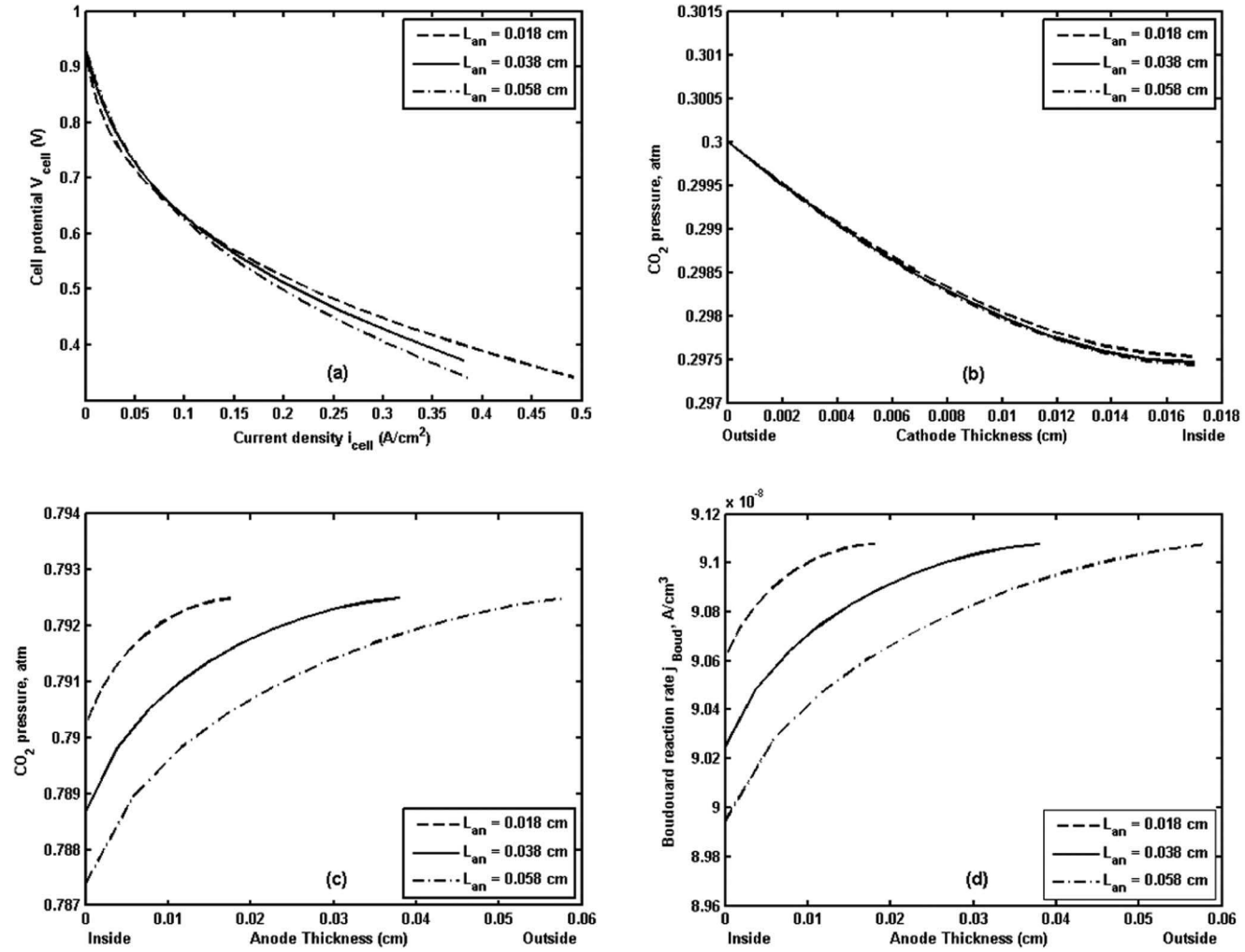

Figure 10. Effect of anode thickness. (a) DCFC performance; (b) Cathode CO_2 distribution at $I_{cell} = 0.2$ A cm^{-2}; (c) Anode CO_2 distribution at $I_{cell} = 0.2$ A cm^{-2}; (d) Anode Boudouard reaction rate distribution at $I_{cell} = 0.2$ A cm^{-2}.

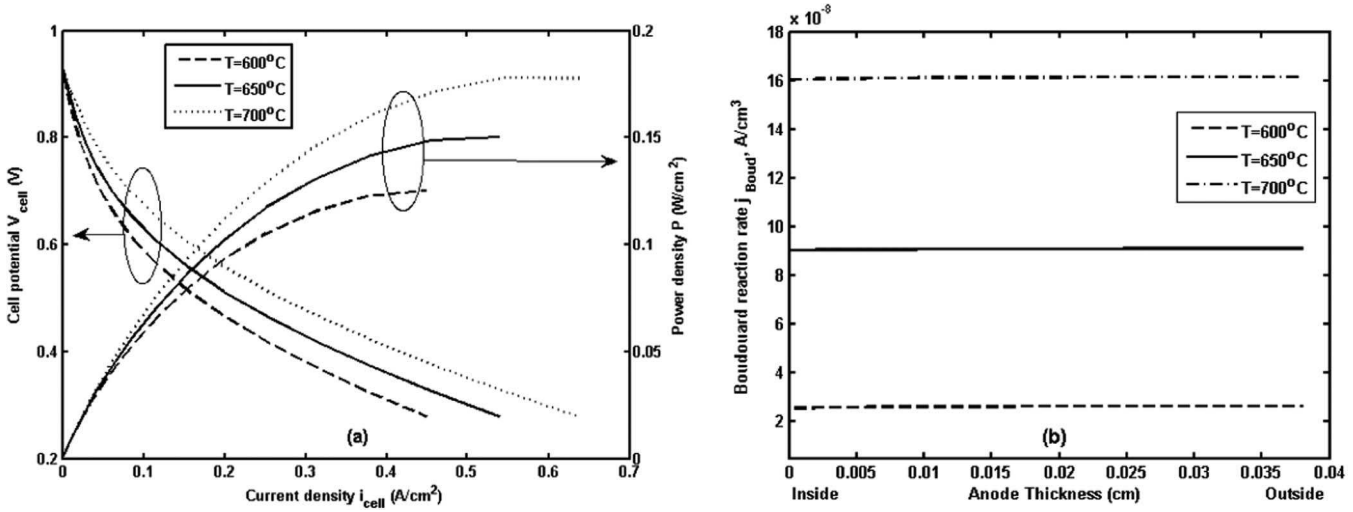

Figure 11. Effects of temperature. (a) DCFC performance; (b) Boudouard reaction rate.

and 10d, respectively. When the anode thickness increases from 0.01m cm to 0.058 cm, the CO_2 partial pressure remains almost unchanged for the same amount of CO_2 requirement from the same cathode at the fixed current density output of 0.2 Acm^{-2}, as shown in Figure 10b. The CO_2 partial pressure distribution in the anode shown in Figure 10c lowers significantly as the anode thickness increases because the volume becomes much larger. The Boudouard reaction rate distributions for different anode thicknesses are determined by the CO_2 distributions in the anode, therefore follows the same pattern of CO_2 partial pressure distributions and are shown in Figure 10d.

Effect of cell temperature.—The effects of cell temperature on DCFC performance are shown in Figure 11a. It can be seen that DCFC performance is significantly influenced by operating temperature. If the cell operates at 0.7V, the current density will almost double from 48mA/cm^2 at 600°C to 85mA/cm^2 at 700°C. The maximum power density increases from 0.125 W/cm^2 at 600°C, to 0.15 W/cm^2 at 650°C and 0.178 W/cm^2 at 700°C. At a current density of 0.2 A/cm^2, the cell voltage increases from 0.466V at 600°C to 0.512V at 650°C and 0.559V at 700°C. The Boudouard reaction rate is calculated using Eq. 32 where the CO_2 partial pressure at the Boudouard equilibrium depends highly on the operating temperature through Eqs. 35 and 36. The Boudouard reaction rate distributions at the three operating temperatures are plotted in Figure 11b. It can be seen that the Boudouard reaction rate jumped from $\sim 2.6 \times 10^{-8}$ A cm^{-3} at 600°C to $\sim 9.1 \times 10^{-8}$ A cm^{-3} at 650°C, and then to $\sim 16.1 \times 10^{-8}$ A cm^{-3} at 700°C.

Table II presents in detail the calculation results of ohmic losses and overpotentials in the electrodes and in the electrolyte matrix at a current density of 0.2A/cm^2 for these three temperatures. It is clear that cell performance improvement can mainly be attributed to reduction of overpotential from the anode and reduced ohmic losses from the electrolyte phase of the electrodes and the electrolyte matrix. Thus, anode performance is more sensitive to temperature, which indicates that anode carbon oxidation has a higher activation energy than the cathode process. A higher operating temperature enhances DCFC performance. However, a higher temperature will favor the reverse Bourdard reaction, as shown in Figure 11b, so producing a higher molar ratio of CO. This is detrimental to electrode materials, fuel utilization and downstream treatment of the anode gas products.

Conclusions

A 1D homogeneous mathematical model was developed for the molten carbonate direct carbon fuel cell. This unit cell model considers the two anodic electrochemical reactions, the 4-electron carbon oxidation and the 2-electron CO oxidation, as well as the reverse Boudouard reaction. The model is validated by comparing the simulated polarization curve with test data from published literature. With the constructed model, parametric studies were conducted to understand the limiting steps in the electrodes and to explore performance optimization for different electrode material volume fractions. It was found that, besides the slow anodic kinetics, ohmic losses in both the anode and the electrolyte matrix significantly reduced DCFC performance. Further modeling exploration revealed that an effective electronic conductivity of 0.56 S/cm in the cathode is sufficient for making high performance DCFCs. By changing the volume fractions of the materials in both electrodes, the model showed that optimal volume fractions exist for the anode materials and, under the given parameter values, the optimal volume fractions of the carbon fuel and the liquid electrolyte in the anode are 0.45 and 0.15, respectively. For the cathode, with an effective electronic conductivity of 0.56 S/cm, optimal volume fractions also exist. The optimal volume fractions of lithiated NiO and liquid electrolyte in the cathode are 0.23 and 0.37 respectively. Model simulation also found that electrode thickness greatly influences DCFC performance. Under the given parameters, increasing cathode thickness to a certain level will improve cell performance, beyond which it levels off. Increasing the electrolyte matrix thickness

Table II. Calculated overpotentials and ohmic losses in each component of the DCFC at $i_{cell} = 0.2$ A/cm^2.

		$(IR)_{ca}$ (mV)			$(IR)_{an}$ (mV)		
T (°C)	η_{ca} (mV)	In solid	In liquid	$(IR)_{el}$ (mV)	In solid	In liquid	η_{an} (mV)
600	−57.24	31.86	35.99	99.81	23.36	140.56	131.89
650	−59.04	30.98	31.49	86.96	22.99	127.93	113.53
700	−60.79	30.45	27.93	77.48	22.68	120.22	85.97

decreases cell performance. Increasing the anode thickness improves cell performance at low current densities but decreases performance at high current densities. Increasing cell operating temperature significantly improves DCFC performance by improving anodic kinetics and effective electrolyte conductivity. Therefore, to achieve high cell performance below 700°C, it is important to focus on the anode material and on structure optimization. Modeling results show that improving the effective ionic conductivity of the anode, the cathode, and the electrolyte matrix will be the key to creating high performance molten carbonate DCFCs.

This 1D unit cell model is a useful tool for gaining insight into the limiting factors of DCFC performance and for conducting parametric studies for the electrodes and for DCFC configuration design and optimization.

List of Symbols

a_C	activity of carbon
d_{el}	exponential correction factor for conductivity in electrolyte
d_{so}	exponential correction factor for conductivity in solid phase
$D^{eff}_{O_2,ca}$	effective diffusivity of dissolved O_2 in the cathode, cm^2/s
$D^{eff}_{CO_2,ca}$	effective diffusivity of dissolved CO_2 in the cathode, cm^2/s
$D_{O_2,ca}$	diffusivity of O_2 in the gas mixture of cathode, cm^2/s
$D_{CO_2,ca}$	diffusivity of CO_2 in the gas mixture of cathode, cm^2/s
$D^{eff}_{CO_2,an}$	effective diffusivity of CO_2 in the anode
$D^{eff}_{CO,an}$	effective diffusivity of CO in the anode
$D_{O_2\text{-}CO_2}$	binary diffusivity of O_2 and CO_2, cm^2/s
$D_{O_2\text{-}N_2}$	binary diffusivity of O_2 and N_2, cm^2/s
$D_{CO_2\text{-}N_2}$	binary diffusivity of CO_2 and N_2, cm^2/s
$D_{CO_2\text{-}CO}$	binary diffusivity of CO_2 and CO, cm^2/s
$D_{X\text{-}Y}$	binary gas phase diffusivity of species X and Y, cm^2/s
E_B	temperature activation of the backward reaction in anode, K
$E_{eq,ca}$	equilibrium potential in the cathode reaction, V
$E_{eq,an,E2}$	equilibrium potential in the anode Reaction 2, V
$E_{eq,an,E4}$	equilibrium potential in the anode Reaction 4, V
E_{s,O_2}	parameter used in Eq. 18 for O_2 solubility calculation
E_{s,CO_2}	parameter used in Eq. 19 for CO_2 solubility calculation
E_{el}	parameter used in Eq. 45, J/mol
F	Faraday's constant, C/mol
i^0_{ca}	exchange current density, A/cm^2
$i^0_{0,ca}$	cathode standard exchange current density, A/cm^2
$i^0_{an,E2}$	exchange current density in the anode for Reaction 2, A/cm^2
$i^0_{an,E4}$	exchange current density in the anode for Reaction 4, A/cm^2
i_{cell}	cell current density, A/cm^2
$j_{an,E2}$	reaction rate in the anode Reaction 2, A/cm^3
$j_{an,E4}$	reaction rate in the anode Reaction 4, A/cm^3
j_{Boud}	reaction rate of the reverse Boudouard Reaction 3, A/cm^3
j_{ca}	reaction rate in the cathode, A/cm^3
K_{0,CO_2}	reference solubility of CO_2 used in Eq. 19, $mol/(cm^3 atm)$
K_{0,O_2}	reference solubility of O_2 used in Eq. 18, $mol/(cm^3 atm)$
K_B	pre-exponential factor of the backward reaction in anode, A/cm^2
K_{Boud}	rate constant of Boudouard Reaction 3, mol/(g atm s)
K_{CO_2}	solubility of CO_2 in the carbonate electrolyte
K_{O_2}	solubility of O_2 in the carbonate electrolyte
K_p	equilibrium constant of the Boudouard reaction
L_{ca}	cathode thickness, cm
L_{el}	electrolyte layer thickness, cm
L_{an}	anode thickness, cm
M_{O_2}	molecular weight of O_2, g/mol
M_{N_2}	molecular weight of N_2, g/mol
M_{CO_2}	molecular weight of CO_2, g/mol
M_{CO}	molecular weight of CO, g/mol
M_X	molecular weight of species X, g/mol
M_Y	molecular weight of species Y, g/mol
n_{ca}	number of electrons in the cathode reaction
$n_{an,E2}$	number of electrons in the anode Reaction 2
$n_{an,E4}$	number of electrons in the anode Reaction 4
p	total cathode pressure, atm
$p_{CO_2,an}$	CO_2 partial pressures in the anode, atm
p_{CO}	CO partial pressures in the anode, atm
$p^0_{tot,an}$	total pressure at the anode inlet, atm
$p^0_{CO_2,an}$	CO_2 partial pressure at the anode inlet, atm
$p^0_{CO,an}$	CO partial pressure at the anode inlet, atm
$p^0_{tot,ca}$	total pressure at the cathode inlet, atm
$p^0_{CO_2,ca}$	CO_2 pressure at the cathode inlet, atm
$p^0_{O_2,ca}$	O_2 pressure at the cathode inlet, atm
p_{O_2}	O_2 gas pressures in the cathode
$p_{CO_2,ca}$	CO_2 gas pressures in the cathode
$p^{el}_{CO_2,ca}$	pressure of the dissolved CO_2 in cathode, atm
$p^{el}_{O_2,ca}$	pressure of the dissolved O_2 in cathode, atm
$p_{CO,Boud}$	partial pressure of CO at Boudouard equilibrium, atm
$p_{CO_2,Boud}$	partial pressure of CO_2 at Boudouard equilibrium, atm
$p_{tot,an}$	total gas pressure of the anode, atm
$p_{tot,ca}$	total gas pressure of the cathode, atm
r_1	cathode reaction parameter in Eq. 15
r_2	cathode reaction parameter in Eq. 15
R	gas constant, J/(molK)
$S_{an,E2}$	reaction surface area per volume in the anode for Reaction 2, cm^2/cm^3
$S_{an,E4}$	reaction surface area per volume in the anode for Reaction 4, cm^2/cm^3
S_{ca}	reaction surface area per volume in the cathode, cm^2/cm^3
T	cell temperature, K
v	average velocity of bubbles in the anode, cm/s
V_{OCV}	open circuit voltage, V
V_{cell}	cell potential, V
W_C	mass concentration of carbon in anode
x	model coordinate, cm
X, Y	represents gas species in the anode or cathode
y_{O_2}	mole fraction of O_2 in cathode
y_{CO_2}	mole fraction of CO_2 in cathode
y_{N_2}	mole fraction of nitrogen in cathode

Greek

$\alpha_{an,E2}$	anode charge transfer coefficient for Reaction 2
$\alpha_{an,E4}$	anode charge transfer coefficient for Reaction 4
α_{ca}	cathode charge transfer coefficient
$\varepsilon_{g,an}$	anode porosity
$\varepsilon_{g,ca}$	cathode porosity
$\varepsilon_{l,el}$	liquid porosity of electrolyte matrix
$\varepsilon_{so,an}$	solid phase volume fraction in anode
$\varepsilon_{so,ca}$	solid phase volume fraction in cathode
$\eta_{an,E2}$	anode overpotential in Reaction 2, V
$\eta_{an,E4}$	anode overpotential in Reaction 4, V
η_{ca}	cathode overpotential, V
ρ_C	density of the carbon in the anode, g/cm^3
σ_C	conductivity of needle coke carbon, S/cm
σ_{el}	bulk ionic conductivity in electrolyte, S/cm
σ^0_{el}	parameter used in Eq. 45, S/cm
σ^{eff}_{el}	effective ionic conductivity in electrolyte matrix, S/cm
$\sigma^{eff}_{el,ca}$	effective ionic conductivity in cathode, S/cm
$\sigma^{eff}_{el,an}$	effective ionic conductivity in anode, S/cm
σ_{LiNiO}	conductivity coefficient of lithiated NiO, S/cm
$\sigma^{eff}_{so,ca}$	effective electric conductivity in cathode, S/cm
$\sigma^{eff}_{so,an}$	effective electric conductivity in anode, S/cm
ϕ_{el}	ionic potential in the electrolyte phase, V

ϕ_{so}	solid phase electric potential, V
$\phi_{so,an}$	electric potential in the anode, V
$\phi_{so,ca}$	electric potential in the cathode, V
ΔG	Gibbs free energy
ΔH_{CO}	enthalpy of reaction of $2C+O_2 \rightarrow 2CO$, kJ/mol
ΔH_{CO_2}	enthalpy of reaction of $C+O_2 \rightarrow CO_2$, kJ/mol
ΔS_{CO}	entropy of reaction of $2C+O_2 \rightarrow 2CO$, kJ/(mol K)
ΔS_{CO_2}	entropy of reaction of $C+O_2 \rightarrow CO_2$, kJ/(mol K)
$(\sum \nu)_{O_2}$	molecular volume of O_2, cm^3
$(\sum \nu)_{N_2}$	molecular volume of N_2, cm^3
$(\sum \nu)_{CO_2}$	molecular volume of CO_2, cm^3
$(\sum \nu)_{CO}$	molecular volume of CO, cm^3

Superscripts and Subscripts

an	anode
ca	cathode
eff	effective value
el	electrolyte phase
eq	equilibrium potential
so	solid phase
tot	total pressure

ORCID

Zhong Xie https://orcid.org/0000-0002-6818-7807

References

1. T. M. Gur, *Chemical Reviews*, **113**, 6179 (2013).
2. S. Giddey, S. P. S. Badwal, and A. K. C. Munnings, *Progress in Energy and Combustion Science*, **38**, 360 (2012).
3. E. J. Carlson, EPRI report. Palo Alto: EPRI; CA 1013362, 2006.
4. C. Jiang, J. Ma, G. Corre, S. L. Jain, and J. T. S. Irvine, *Chem. Soc. Rev.*, **46**, 2889 (2017).
5. T. Cao, K. Huang, Y. Shi, and N. Cai, *Energy & Environmental Science*, **10**, 460 (2017).
6. A. Elleuch, A. Boussetta, and K. Halouani, *Journal of Electroanalytical Chemistry*, **668**, 99 (2012).
7. J. Zhang, X. Jiang, G. Piao, H. Yang, and Z. Zhong, *International Journal of Hydrogen Energy*, **40**, 3321 (2015).
8. L. Xing, J. Hao, X. Li, Y. Zhang, Z. Hu, and Y. Gao, *Journal of Power Sources*, **363**, 428 (2017).
9. S. Eom, S. Ahn, K. Kang, and G. Choi, *Journal of Power Sources*, **372**, 54 (2017).
10. Q. Liu, Y. Tian, C. Xia, L. T. Thompson, B. Liang, and Y. Li, *Journal of Power Sources*, **185**, 1022 (2008).
11. H. Li, Q. Liu, and Y. Li, *Electrochimica Acta*, **55**, 1958 (2010).
12. B. R. Alexander, R. E. Mitchell, and T. M. Gur, *Proceedings of the Combustion Institute*, **34**, 3445 (2013).
13. A. Elleuch, M. Sahraoui, A. Boussetta, K. Halouani, and Y. Li, *Journal of Power Sources*, **248**, 44 (2014).
14. R. Agarwal, *Ph.D. Thesis*, Virginia Polytechnic Institute and State University, 2014.
15. C.-C. Chen and J. R. Selman, *Journal of Power Sources*, **353**, 312 (2017).
16. C. C. Chen and J. R. Selman, *ECS Transactions*, **28**, 31 (2010).
17. K. Maheshwari, A. Sen, and B. Krishnamurthy, *International Journal of Hydrogen Energy*, **43**, 20077 (2018).
18. R. K. Mohammed and B. Krishnamurthy, *Journal of Electroanalytical Chemistry*, **834**, 167 (2019).
19. Y. Nabae, K. D. Pointon, and J. T. S. Irvine, *Energy & Environmental Science*, **1**, 148 (2008).
20. T. M. Gur, *Journal of The Electrochemical Society*, **157**, B751 (2010).
21. W. H. A. Peelen, M. Olivry, S. F. Au, J. D. Fehribach, and K. Hemmes, *Journal of Applied Electrochemistry*, **30**, 1389 (2000).
22. J. F. Cooper and J. R. Selman, *International Journal of Hydrogen Energy*, **37**, 19319 (2012).
23. J. R. Welty, C. E. Wicks, R. E. Wilson, and G. L. Rorrer, *Fundamentals of Momentum, Heat, and Mass Transfer*, 5th Edition ed., John Wiley & Sons, Inc., 2008.
24. E. N. Fuller, P. D. Schettler, and J. K. Giddings, *Industrial and Engineering Chemistry*, **58**, 18 (1966).
25. A. Boden and G. Lindbergh, *Journal of The Electrochemical Society*, **153**, A2111 (2006).
26. J. A. Prins-Jansen, K. Hemmes, and H. W. de Wit, *Electrochimica Acta*, **42**, 3585 (1997).
27. G. Wilemski, *Journal of The Electrochemical Society*, **130**, 117 (1983).
28. T. Kojima, Y. Miyazaki, K. Nomura, and K. Tanimoto, *Journal of The Electrochemical Society*, **154**, F222 (2007).
29. M. Chen, C. Wang, X. Niu, S. Zhao, J. Tang, and B. Zhu, *International Journal of Hydrogen Energy*, **35**, 2732 (2010).
30. N. Subramanian, B. S. Haran, R. E. White, and B. N. Popov, *Journal of The Electrochemical Society*, **150**, A1360 (2003).
31. T. B. Reed, *Free Energy of Formation of Binary Compounds*, MIT Press, Cambridge, Mass., 1971.
32. H.-J. Choi, S.-K. Ihm, T.-H. Lim, and S.-A. Hong, *Journal of Power Sources*, **61**, 239 (1996).
33. M. Doyle, J. Newman, A. S. Gozdz, C. N. Schmutz, and J.-M. Tarascon, *Journal of The Electrochemical Society*, **143**, 1890 (1996).
34. J. Larminie and A. Dicks, *Fuel Cell Systems Explained*, John Wiley & Sons, Ltd., 2002.
35. A. Wijayasinghe, *Ph.D. Thesis*, Royal Institute of Technology, Stockholm, 2004.